
A Polar-Drive Shock-Ignition Design for the National Ignition Facility

Introduction

In direct-drive inertial confinement fusion (ICF),¹ a small spherical capsule filled with a deuterium–tritium (DT) mix is imploded by irradiating the capsule symmetrically with high-intensity lasers to achieve a high-density, high-temperature state where fusion reactions may readily occur. The capsule shell is accelerated by the ablation pressure of the laser-heated plasma at the outer edge of the shell to high velocity ($v_{\text{imp}} > 3.5 \times 10^7$ cm/s, where v_{imp} is the implosion velocity), compressing the capsule to a high density. As the capsule implodes, the back pressure from the compressed plasma in the center of the capsule slows the implosion until the shell stagnates. At stagnation, the fill gas has been compressed and heated via shocks and adiabatic compression, forming a low-density central hot spot surrounded by a dense shell tamper consisting of DT fuel. If sufficient hot-spot temperature (≥ 10 keV) and shell areal density ($\rho R \equiv \int_0^\infty \rho dr \geq 0.3$ g/cm²) are achieved, energetic alpha particles created by the hot-spot fusion reactions are stopped in the cold dense shell, heating it quickly, and initiating ignition, which causes the fusion reaction rate to rise dramatically, burning a substantial portion of the DT fuel.

Shock ignition (SI)² is a relatively new concept in which the compression phase and ignition phase are separated.³ Practically, this separation is achieved by dividing the laser pulse into two parts: a main-drive or compression pulse, and a spike or ignition pulse timed at the end of the main pulse. The main-drive pulse is typically of lower power than in hot-spot direct drive since the main pulse serves solely to compress the shell to the required areal density for ignition and not to heat the hot spot. This lower drive power corresponds to a lower implosion velocity, typically less than 3.0×10^7 cm/s. At the end of the main pulse, an intense spike pulse launches a strong shock through the imploding shell material to heat the hot spot quickly to ignition temperatures.

By separating the compression from the hot-spot heating, SI somewhat resembles the fast-ignition concept.⁴ However, SI requires a spherically symmetric laser illumination of much more moderate laser intensity (typically several times

10^{15} W/cm²) than is required for fast ignition ($> 10^{19}$ W/cm²), such that the SI heating pulse can be generated with the same laser system as the main-drive pulse. In contrast, fast ignition requires chirped-pulse amplification to generate pulses of high intensity. Furthermore, SI heating is accomplished via shock heating, which is well understood and easily modeled, as opposed to fast ignition, which delivers energy via the generation and transport of relativistic fast electrons, which is difficult to model theoretically or computationally.

Achieving ignition through SI is not without its uncertainties. For SI to be viable, laser-generated strong shocks of the order of 300 Mbar must be demonstrated experimentally in a spherical geometry. Furthermore, at these intensities, laser–plasma interactions (LPI’s) become significant and can greatly influence the coupling of laser energy to the imploding capsule, affecting the strong-shock formation and potentially preheating the cold fuel prior to full capsule compression. An experimental understanding of LPI in this intensity regime, therefore, is very important in predicting the success of SI implosions.

It should be noted that a concept similar to SI was proposed a few decades ago by Shcherbakov.⁵ The concept proposed at that time, however, called for much lower initial compression velocities $v_{\text{imp}} \simeq 2.0 \times 10^6$ cm/s (the final velocity after the shock pulse is quoted as $v_{\text{imp}} \simeq 1.5 \times 10^7$ cm/s). The laser drive needed to compress and shock the capsule in that design was not specified, and only the absorbed laser energy $E \simeq 30$ kJ was cited. An article by the same author two decades later⁶ indicates laser-drive parameters of $P \simeq 10$ TW, $I \simeq 10^{13}$ W/cm², and $\Delta t_{\text{pulse}} \simeq$ tens of nanoseconds, with shock laser parameters of $P \simeq 10$ PW, $I \simeq 10^{16}$ W/cm², and $\Delta t_{\text{pulse}} \simeq$ a few hundreds of picoseconds. This work, therefore, seems to indicate very different regimes of both laser operation and capsule design relative to the conceptual paper of Betti *et al.*² even though the concept is essentially the same.

Research in SI^{7–30} has garnered much interest both experimentally and theoretically in the international fusion community over the past several years. Theoretical models,^{7–10} scaling

laws,^{7,11–16} and computational target designs in one dimension (1-D)^{11,13,14,17,18} and multiple dimensions^{13–15,18–20} have investigated the feasibility of SI on a variety of target platforms. These studies have validated the claims of Betti *et al.*² that the addition of a strong shock reduces the energy required for ignition, allowing for higher gain at a given input laser energy. Strong-shock propagation experiments in planar²¹ and spherical geometry²² have validated computation modeling of shocks driven at intensities up to 1.5×10^{15} W/cm². Full-implosion experiments²³ have been performed on OMEGA²⁴ showing increased neutron yield, areal density, and yield-over-clean (defined as the ratio of the experimental yield to 1-D simulated predictions) relative to similar no-spike experiments. Particle-in-cell LPI simulations of OMEGA experiments²⁵ and full-scale ignition designs²⁶ have reported hot-electron generation in the temperature regime up to 40 keV at SI-relevant laser intensities with total reflectivities (Raman and Brillouin scattering) from 10% to 35% of the incident laser energy. Spherical LPI experiments^{27,28} performed on OMEGA at SI-relevant intensities and plasma conditions have resulted in similar findings. Planar LPI experiments²⁹ have also been performed in France. The hot-electron temperatures reported in these simulations and experiments appear favorable for SI in light of computational investigations of hot-electron coupling during spike propagation,³⁰ which report enhanced strong-shock pressures and higher ignition margin as a result of hot-electron energy coupling at electron temperatures up to 100 keV. All of these studies indicate that the SI method is a viable path to achieve ignition and gain in ICF.

Most of the theoretical research published to date has been limited to either conceptual designs or designs for proposed laser facilities or facilities still under construction. This article proposes a design for experiments on the currently operational National Ignition Facility (NIF).³¹ These proposed experiments conform to the NIF system specifications and could be fielded in the polar-drive configuration on the NIF within the next several years, requiring only minor system modifications. Such modifications include the design and manufacture of specifically tailored phase plates;^{32,33} implementation of multifrequency-modulation smoothing by spectral dispersion (multi-FM SSD)^{34,35} in NIF beamlines; design and introduction of polarization plates for polarization smoothing; and the development of a polar-drive target insertion cryostat.

This article is organized as follows: A theoretical model for calculating target robustness is outlined; a 1-D target design for the NIF is developed and implosion robustness to 1-D physics and system uncertainties is detailed; and a polar-drive

beam configuration for the NIF is outlined and robustness to two-dimensional (2-D) drive and capsule nonuniformities is explored. The capsule is found to robustly ignite under all anticipated sources of 1-D uncertainty and 2-D perturbations.

Characterizing Robustness

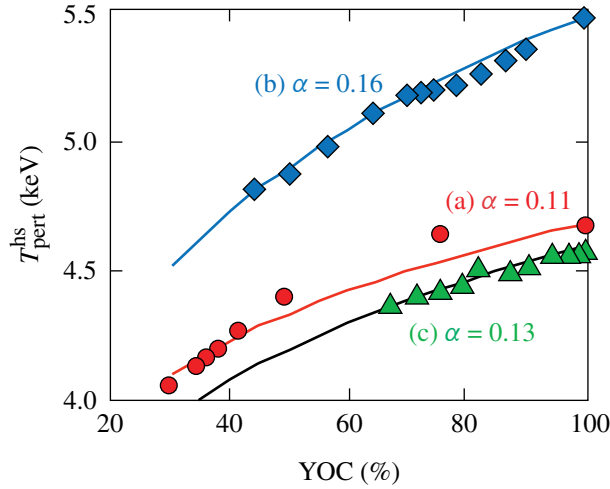
In ICF target design, it is important to characterize design performance. Often in the ICF community, 1-D target gain has been used as a metric to preferentially guide target design. One-dimensional gain in an igniting target, however, is largely a function of the assembled fuel areal density (see Ref. 1, p. 40) and, as a metric for target design, does not provide a reference for how close the target implosion is to the ignition threshold. It is therefore important to define a metric for the margin of error, in a 1-D sense, to quantify the robustness of the proposed shock-ignition design for the NIF. In this article, target designs will be characterized using the ignition threshold factor (ITF).^{36–38} By the definition of ITF as described in Spears *et al.*,³⁸ an ITF of 1 corresponds to an ~50% chance of ignition with the DT target in simulations.

In this article, the ITF is calculated in 1-D simulations using the methodology of Chang *et al.*³⁷ Essentially, the fusion reactivity rate $\langle\sigma\nu\rangle$ of the DT fuel is artificially reduced by a variable parameter in the simulation

$$\langle\sigma\nu\rangle_{\text{mod}} = \xi\langle\sigma\nu\rangle \quad (1)$$

until the target yield degrades to a gain of 1, where the fusion output energy equals the input laser energy. Here $\langle\sigma\nu\rangle_{\text{mod}}$ is the modified fusion reactivity rate, and ξ is the fractional input parameter. This is analogous to multiplying the neutron yield obtained in the absence of alpha-particle heating by the same factor. One may characterize this input parameter ξ as a clean-volume fraction, defined as the fraction of the 1-D hot-spot volume $\xi = V_{3\text{-D}}^{\text{hs}}/V_{1\text{-D}}^{\text{hs}}$, where $V_{3\text{-D}}^{\text{hs}}$ is the clean hot-spot volume in three dimensions (3-D) varied as an input parameter and $V_{1\text{-D}}^{\text{hs}}$ is the 1-D hot-spot volume.

In simple models of clean volume fraction, the yield-over-clean (YOC), which is defined as the 3-D yield divided by the 1-D yield ($\text{YOC} \equiv Y_{3\text{-D}}/Y_{1\text{-D}}$), is typically equated to the clean-volume fraction. These models, however, ignore the effect of shell perturbations on the hot-spot temperature. Two-dimensional DRACO³⁹ simulations of three igniting targets, described in Fig. 3 of Ref. 37 with varying levels of input nonuniformity, are used to evaluate the functional dependence of the hot-spot ion temperature on the YOC. In Fig. 133.1, the neutron-averaged ion temperature is plotted for these three



TC10412JR

Figure 133.1

Relation of the hot-spot temperature ($T_{\text{pert}}^{\text{hs}}$) to the yield-over-clean (YOC), as calculated by 2-D DRACO simulations for the three targets discussed in Fig. 3 of Ref. 37. Power-law fits to each of these are shown as solid lines with power-law exponents varying from 0.11 to 0.16.

targets [labeled (a), (b), and (c), as in Ref. 37] versus the no-burn YOC. The perturbed, hot-spot ion temperature for each of these designs is shown to scale roughly as a weak power-law function of the YOC:

$$T_{\text{pert}}^{\text{hs}}(\text{YOC}) = T_{1\text{-D}}^{\text{hs}} \cdot \text{YOC}^{\alpha}, \quad (2)$$

as shown by the continuous lines of Fig. 133.1. The power-law exponent α was found to vary from 0.11 to 0.16 in the different designs. Here, we will assume an average value of 0.13 for α .

We employ a simple model of the hot spot, which assumes a single temperature over the hot-spot volume

$$\text{YOC} = \frac{Y_{3\text{-D}}}{Y_{1\text{-D}}} = \xi \left(\frac{T_{3\text{-D}}^{\text{hs}}}{T_{1\text{-D}}^{\text{hs}}} \right)^{\beta}, \quad (3)$$

where $T_{3\text{-D}}^{\text{hs}}$ is the perturbed hot-spot ion temperature and $T_{1\text{-D}}^{\text{hs}}$ is the 1-D hot-spot ion temperature. The fusion reactivity in the hot spot is assumed to scale as a power law⁴⁰ in the temperature over the temperatures of interest, with $\beta = 2$.

Using the formula for the χ parameter from Eq. (12) of Ref. 37,

$$\chi = \left[\rho R (\text{g/cm}^2) \right]^{0.8} (T/4.7 \text{ keV})^{1.7} (\text{YOC})^{0.5}, \quad (4)$$

the scalings for areal density ρR and hot-spot ion temperature from Eqs. (19) and (52), respectively, of Ref. 41,

$$\rho R_{\text{shell}} \sim E_{\text{kin}}^{0.33} \quad (5)$$

and

$$T_{\text{hs}} \sim E_{\text{kin}}^{0.07}, \quad (6)$$

and defining the ITF as the ratio of the kinetic energy E_{kin} of the imploding shell to the minimum energy required to ignite the same shell, one obtains a scaling relation between χ and the ITF,

$$\text{ITF} \sim \chi^{2.6}. \quad (7)$$

Substituting Eqs. (2)–(4) into Eq. (7) yields

$$\text{ITF} \sim \xi^{1.5}. \quad (8)$$

When a series of 1-D simulations with alpha-energy transport are performed, varying the clean-volume fraction ξ , one finds a critical value of ξ , below which ignition is quenched. We will term this the minimum clean-volume fraction required for ignition $\xi_{\text{min}}^{\text{ign}}$, which corresponds to an ITF of 1. Using $\xi_{\text{min}}^{\text{ign}}$, one can rewrite Eq. (8) for the 1-D ITF as

$$\text{ITF}_{1\text{-D}} \simeq (\xi_{\text{min}}^{\text{ign}})^{-1.5}. \quad (9)$$

In this article, we will use Eq. (9) to determine the 1-D robustness of our target design.

One-Dimensional Target Design and Robustness Studies

This section outlines the NIF SI target design in 1-D and details the robustness of the target to various sources of physics and system uncertainties. In designing a shock-ignition target for the NIF, the most-constraining system limitation is the total system's peak laser power. The early SI design at 290 kJ proposed by Betti *et al.*² used a laser spike with a peak laser power of 540 TW. Scaling this target to NIF's total energy of ~ 1.5 MJ, the required laser power reaches ~ 1600 TW, prohibitively high for the NIF, which recently achieved⁴² a peak power of 520 TW. Indeed, Betti's design at 290 kJ already exceeds the demonstrated NIF peak power. Therefore, some modifications to the conceptual design must be made for experiments on the NIF. The first is to scale only to sub-MJ laser energy to allow for more headroom in power space. The second is to raise the capsule's implosion velocity by making the shell thinner. This recovers the stagnation pressure and temperature that is lost

when simply reducing the laser power to conform to the NIF’s power ceiling. Additional robustness is achieved by allowing that the laser pulse may be split, such that half of the NIF beams drive the target compression and are focused at the original target radius, while the other half drive the spike shock using more tightly focused beams to improve energy coupling to the target late in time. All 1-D simulations in this article were performed using the radiation–hydrodynamics code *LILAC*⁴³ with the *SESAME*⁴⁴ equation of state and a flux-limited Spitzer heat conductivity⁴⁵ with a flux-limiter value of 0.06.

The target design chosen is shown in Fig. 133.2. The capsule has a 1080- μm radius with a 161- μm solid-DT fuel layer surrounded by a 31- μm outer plastic ablator layer. The ablator thickness is chosen such that the ablator material is fully ablated by the end of the laser pulse to mitigate deceleration-phase mixing of the plastic with the DT fuel. The total energy delivered by the laser is 689 kJ, divided into two pulses, as shown in Fig. 133.3. The main pulse shown by the solid line contains a total of 544 kJ and has a laser profile characterized as a super-Gaussian intensity profile $I(r) = \exp\left[-(r/r_0)^\sigma\right]$ with a $1/e$ radius $r_0 = 677 \mu\text{m}$ and super-Gaussian exponent $\sigma = 2.5$. The spike pulse (dashed line) contains a total of 145 kJ with a peak power of 215 TW, also in a super-Gaussian spot of $r_0 = 258 \mu\text{m}$ and $\sigma = 2.5$.

As seen in Fig. 133.3, the laser pulse design has two “picket” pulses at the beginning, followed by a low-intensity foot with a slow rise to the main compression drive, and ultimately concluding with a spike pulse at the end of the main compression.

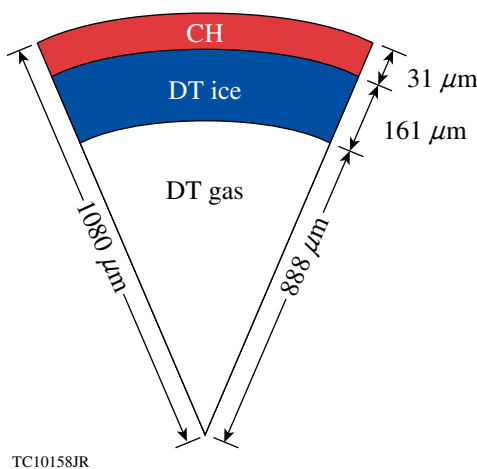


Figure 133.2
Capsule dimensions for the NIF shock-ignition (SI) design.

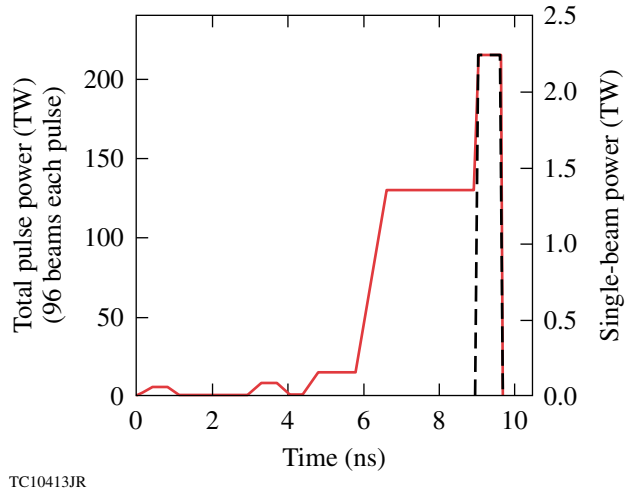


Figure 133.3
Laser pulse history for the main drive beams (solid red) and spike beams (dashed black) comprising the 1-D SI laser pulse design.

The picket pulses serve two purposes: The first is to raise the ablation velocity^{46–49} $v_{\text{abl}} = \dot{m}/\rho_{\text{abl}}$ (where v_{abl} is the ablation velocity, \dot{m} is the mass ablation rate, and ρ_{abl} is the density at the ablation front) to reduce the growth of the Rayleigh–Taylor (RT) instability,^{50,51} which is a major obstacle to ICF. This ablative stabilization of the RT instability has been demonstrated theoretically^{52–54} and experimentally.⁵⁵ The second purpose of the picket pulses is to facilitate simplified shock tuning and adiabat control.⁵⁶

The ramp times of the pickets and foot of the main drive are chosen as 400-ps linear ramps to account for a 350-ps spatiotemporal skew in the NIF beamlines that is introduced by the diffraction grating required for 1-D multi-FM SSD.⁵⁷ Shorter, more-intense pickets would more efficiently reduce laser imprint^{58–65} and provide increased adiabat shaping⁴⁸ for multidimensional stability, but such pickets are not currently possible on the NIF. The flattop of each picket pulse is also 400 ps, chosen to facilitate better SSD smoothing.^{57,66} This allows for a longer time when the laser pickets are at their highest power and while the beams fill the full aperture of the phase plates. The ramp time from the main drive to the spike pulse is, by design, 100 ps; however, 1-D simulations indicate that increasing the rise time to 400 ps (fixing the center of the rise in time) still gives full 1-D gain with the same $\text{ITF}_{1\text{-D}}$; i.e., no margin is lost.

The compression pulse launches four distinct shocks: one by each picket, one by the foot, and one by the ramp to main compression drive. As in previous designs with multiple

shocks,^{48,49,56} the shocks are tuned such that the shocks merge approximately at the rear surface of the solid DT fuel layer. The first picket pulse has a peak 96-beam (single-beam powers in parentheses) power of 6 TW (0.063 TW) and is followed by a second picket, which starts at 2.9 ns and has a peak power of 8 TW (0.083 TW). The foot of the main compression pulse is 15 TW (0.16 TW) beginning at 4.4 ns. Following the foot, the laser pulse rises beginning at $t = 5.8$ ns over 800 ps to a main compression power of 130 TW (1.35 TW). Finally, at $t = 8.95$ ns, the spike pulse begins, rising over 100 ps to 215 TW (2.24 TW). At the same time, the shock beams are turned on using the pulse history shown by the dashed curve, which also peaks at 215 TW (2.24 TW), giving a total system 192-beam peak power of 430 TW—17% below the recently demonstrated achieved peak power⁴² of 520 TW on the NIF. Since both the peak power and individual pulse energies of this design are significantly below the demonstrated capabilities of the NIF, this design offers substantial system headroom for capsule tuning to match experimental and simulated absorption, shell velocity, and spike shock pressure, as well as 2-D polar-drive symmetry.

The result is a mass-averaged in-flight fuel adiabat at the end of the compression drive of $\langle \alpha \rangle_{\text{fuel}} = 1.8$ with a minimum adiabat at the inner edge of the dense shell of $\alpha_{\text{in}} = 1.2$. The adiabat here is characterized using the “DT-standard” adiabat,⁴⁰ which is given by $\alpha_{\text{DT-standard}} = P/(2.18 \rho^{5/3})$, where P is in Mbar and ρ in g/cm^3 . The implosion velocity is $v_{\text{imp}} = 3.05 \times 10^7$ cm/s, which is substantially faster than Betti’s target of Ref. 2. The target achieves a 1-D gain of 58 with a peak areal density $\rho R = 1.6$ g/cm². The in-flight aspect ratio (defined as $\text{IFAR} \equiv R/\Delta R$, where R is the shell radius and ΔR is the shell thickness), calculated when the shell radius is two-thirds of the initial target radius, is 22. Target robustness is excellent with an $\text{ITF}_{1\text{-D}} = 4.1$. These 1-D performance parameters are summarized in Table 133.I.

The effect of the spike shock on target robustness was studied in 1-D by varying the spike laser intensity to alter the applied

Table 133.I: One-dimensional performance characteristics of the NIF shock-ignition design.

Gain	58
ρR (g/cm ²)	1.6
v_{imp} ($\mu\text{m/ns}$)	305
$\text{IFAR}_{2/3}$	22
Average adiabat	1.8
$\text{ITF}_{1\text{-D}}$	4.1

pressure of the spike shock. Figure 133.4 plots the calculated $\text{ITF}_{1\text{-D}}$ as a function of the initial shock pressure near the ablation surface. The nominal shock pressure of the original design is 300 Mbar. The lowest pressure in Fig. 133.4 corresponds to the case where the spike shock is removed entirely. In this case, the pressure reported (160 Mbar) is the ablation pressure. Figure 133.4 shows that this target is predicted to ignite in 1-D even without the spike shock, but with a much lower $\text{ITF}_{1\text{-D}}$ of 1.3. It also shows clearly that additional ignition margin is predicted when the spike pulse is present.

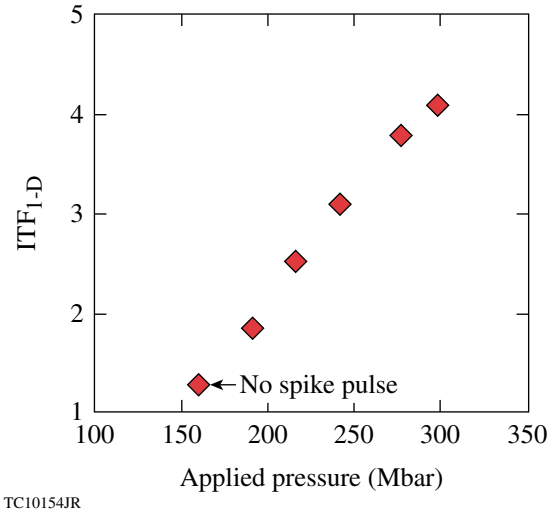
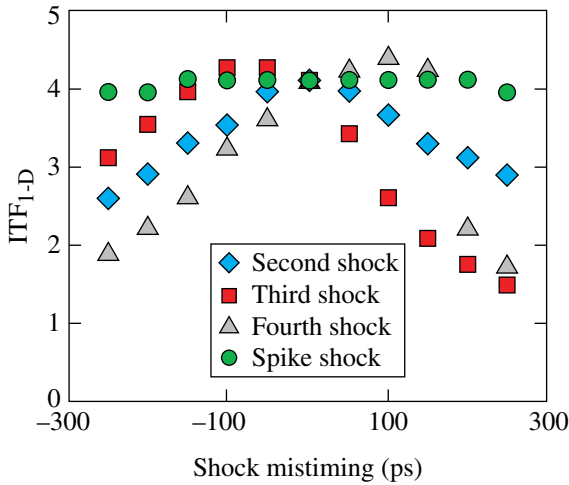


Figure 133.4 Plot of the $\text{ITF}_{1\text{-D}}$ versus the applied pressure in the spike shock. The lowest pressure point corresponds to the ablation pressure with no spike pulse. ITF: ignition threshold factor.

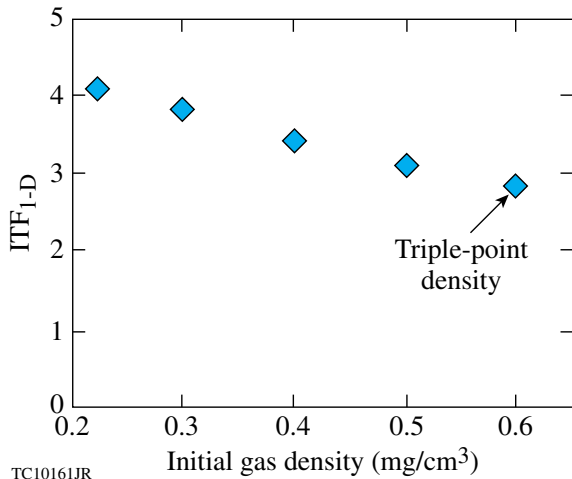
A series of 1-D simulations examined the robustness of the design to systematic mistiming of shocks. Figure 133.5 shows the calculated $\text{ITF}_{1\text{-D}}$ as a function of shock mistiming for the second shock (launched by the second picket), the third shock (launched by the foot of the main pulse), the fourth shock (launched by the ramp to the main compression drive), and the spike-pulse shock. As can be seen from the plots, the design ignites for all mistimings studied and has large timing windows within which a high margin is maintained. For reference, systematic shock mistiming on the NIF is estimated⁶⁷ to be 10 ps.

It is anticipated that such a target would be shot on the NIF at a temperature of 17.8 K, two degrees below the triple point of the DT fuel mixture with an initial gas density of 0.225 mg/cm³. Figure 133.6 illustrates how changing the initial gas density affects the $\text{ITF}_{1\text{-D}}$ in simulations. These data demonstrate the advantage of shooting at a lower temperature and gas density since the $\text{ITF}_{1\text{-D}}$ drops noticeably as the temperature



TC10414JR

Figure 133.5
Plot of the ITF_{1-D} versus shock mistiming for the 1-D capsule design.



TC10161JR

Figure 133.6
 ITF_{1-D} plotted versus the initial gas density in the target.

and gas density increase. It should be noted that the target is still predicted to ignite in 1-D at a gas density near the triple point ($T = 19.8$ K, $\rho_{\text{gas}} = 0.62$ mg/cm³) with an ITF_{1-D} of 2.8.

Since laser-plasma interactions can have a significant impact on ICF implosions, it is important to quantify the laser intensity, plasma temperature, and density scale lengths in the hot corona. Temporally and spatially averaged conditions at the quarter-critical surface are reported in Table 133.II during both the main compression pulse and the spike pulse. The laser intensities reported in this table are “nominal” in the sense that

Table 133.II: Average laser intensity $\langle I_{14} \rangle$ at the quarter-critical radius (units of 10^{14} W/cm²); average density gradient scale length $\langle L_n \rangle$ (μm); electron temperature T_e (keV); and the two-plasmon-decay hot-electron threshold F_{TPD} , calculated by Eq. (10). Values are reported during both the main-drive and spike pulses.

	Main drive	Spike
$\langle I_{14} \rangle$	8	34
$\langle L_n \rangle$ (μm)	350	450
T_e (keV)	3.5	8.5
F_{TPD}	3.5	7.8

they are averaged over the quarter-critical surface. Since the laser spots of the spike beams are much smaller ($1/e$ radius of $258 \mu\text{m}$) compared to the average quarter-critical radius ($\sim 1000 \mu\text{m}$), there will be hot spots of higher laser intensity in some locations.

From these plasma conditions, one can evaluate a two-plasmon-decay (TPD) threshold parameter F_{TPD} during both pulses using the formula⁶⁸

$$F_{\text{TPD}} = \frac{I_{14} L_n}{230 T_e}, \quad (10)$$

where I_{14} is the laser intensity in units of 10^{14} W/cm², L_n is the density gradient scale length in microns, and T_e is the electron temperature in keV. For values of F_{TPD} greater than 1, hot-electron heating from TPD has been reported in OMEGA experiments.^{69,70} The threshold parameter is predicted to be above 1 during both the main-drive and spike pulses, indicating a likelihood of hot-electron generation and preheating during both the compression and shock phases of the implosion. TPD thresholds for NIF targets have not yet been characterized, but thresholds for OMEGA targets have been shown to be dependent on beam geometry.⁷¹ Hot-electron generation during the main-drive pulse caused by TPD may be an issue for this target. If so, one mitigation strategy that has been proposed is the use of higher-Z ablaters, e.g., silicon or glass.^{70,72}

Given the high intensity of the spike pulse, and in light of recent shock-ignition-relevant experiments on OMEGA, it is predicted that during the spike pulse, stimulated Raman scattering (SRS), rather than TPD, will likely be the dominant factor in hot-electron generation.^{28,73,74} The SRS hot-electron temperature in those experiments was shown to be ~ 40 keV with a conversion efficiency of up to $\sim 16\%$ of the incident spike laser energy.

With this in mind, 1-D simulations of hot-electron energy coupling were performed in *LILAC* using a multigroup diffusion model of suprathermal electron energy transport. Various electron temperatures and coupling efficiencies were studied. The results, plotted in Fig. 133.7, show that this SI design is robust to energy coupling from hot electrons with Maxwellian temperatures of up to 150 keV and coupling efficiencies of up to 30%, similar to the results of Ref. 30. Furthermore, an analysis of *LILAC* simulations at hot-electron temperatures above 100 keV suggests a competition between increased shock coupling as a result of the lower-energy hot electrons stopping at the ablation front and volumetric heating of the cold fuel caused by higher-energy hot electrons streaming through the target, increasing the shell adiabat and lowering compressibility. These two effects oppose one another: one to improve target performance, the other to degrade performance. A more-rigorous model of suprathermal electrons is required to more-accurately quantify the effects of hot-electron transport at temperatures above 150 keV.

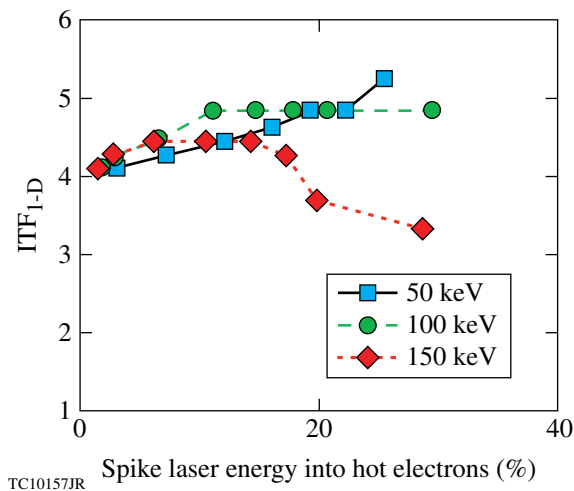


Figure 133.7
ITF_{1-D} plotted with various levels of hot-electron energy coupling during the spike pulse. Energy coupling is varied for different hot-electron temperatures and generation efficiency as a percentage of the spike laser energy.

Two-Dimensional Polar-Drive Configuration and Nonuniformity Studies

Because of the current indirect-drive laser configuration on the NIF, in which the laser beams are clustered near the poles for entry into a vertically oriented hohlraum, it is necessary to devise a scheme that will directly drive a capsule uniformly to preserve shell integrity and hot-spot confinement. Simply pointing all the NIF beams with equal power toward the center of the capsule will result in higher intensities at the poles than at the equator. As such, the equator of the target would be driven

at a slower velocity than the poles, resulting in an unacceptable target asymmetry. In polar drive (PD), beams from the poles and mid-latitudes of the target chamber are deliberately pointed toward the equator of the target to correct for the lower drive intensity there. Hot-spot polar-drive targets have shown promise in both simulations^{75–78} and experiments.^{79,80} While other schemes have been devised in which no repointing is deemed necessary¹⁸ or in which an equatorial ring is used to redirect laser energy toward the equator,^{80,81} they are not investigated in this article.

As mentioned earlier, substantial margin can be regained for SI designs on the NIF by using two separate laser pulses—one to drive the compression and one to shock the capsule. For SI-specific purposes, two separate PD beam-configuration types have been proposed. NIF beams are bundled into groups of four termed “quads.” The first and simplest PD scheme to implement on the NIF is one where half of the NIF’s 48 quads drive the capsule compression and the other half drive the ignitor shock. The other scheme divides the beams within a single quad, using two beams from each of the 48 NIF quads for the compression and the remaining two beams for the shock. Here, we will use the term “full-quad” for the first scheme and “split-quad” for the second. It should be noted that the split-quad scheme requires modifications to the front end of the NIF Laser System to allow different laser pulses to propagate through separate beamlines within a single quad;⁸² therefore, the full-quad scheme is more likely to be used in the near term. However, since much work has been done on PD designs of standard hot-spot capsules for the NIF using 48-quad beam pointings,^{75–77} this article focuses mainly on polar-drive SI using 48 split quads as compression beams to capitalize on lessons learned in a similar beam geometry. Initial results from full-quad, polar-drive SI are also presented.

Modeling the laser deposition computationally in either scheme requires a fully 3-D ray trace. All 2-D PD simulations in this article were performed using the arbitrary Lagrangian–Eulerian radiation–hydrodynamics code *DRACO*.^{39,76} In designing a PD pointing scheme for a specific target, one may use different laser spot shapes and sizes, as well as vary the pulse power from quad to quad until the desired shell uniformity is achieved. The NIF is currently capable of providing separate laser pulse shapes to each quad, and phase plates can be designed to produce specified laser spot shapes and sizes.

A specific split-quad beam-pointing scheme was developed for the compression beams wherein the 48 half-quads, which can be divided into five separate “rings” of beams with the

same port angle, were repointed toward five separate latitudes on the target surface. The beam repointings are summarized in Table 133.III. In this table, the beam port angle describes the location at which the beams enter the target chamber, relative to pole, and the repointing angle on target represents the polar-angle position of the center of the beam on the target surface. All the beams located at the 23.5° and 30° port angles are repointed to the target surface at 24.5° and 44°, respectively, both toward the target equator, and are referred to as Ring 1 and Ring 2 in Table 133.III. Half of the 44.5° quads (Ring 3) are repointed slightly toward the pole to the 44° target angle, and the other half (Ring 4) to the 82° position. Finally, the 50° quads (Ring 5) are all pointed to 82° on target.

Table 133.III: Split-quad polar-drive (PD) beam-repointing angles for the main-drive beams given by beam port location.

	Beam port angle (°)	Repointing angle on target (°)
Ring 1	23.5	24.5
Ring 2	30.0	44.0
Ring 3	44.5	44.0
Ring 4	44.5	82.0
Ring 5	50.0	82.0

In addition, laser-spot profiles for the drive beams were altered from the 1-D spot shapes to better distribute laser absorption and achieve better capsule uniformity and performance. The first alteration is to use a lower super-Gaussian order, reducing it from $\sigma = 2.5$ in the 1-D design to $\sigma = 2.2$. This removes much of the short-wavelength nonuniformity in the absorption. Next, a secondary elliptical spot is superimposed over the circular spots of Rings 4 and 5. This secondary ellipse has an amplitude of 30% relative to the circular spot, an ellipticity of 2.5 with its major axis oriented in the same plane as the target’s equator, a super-Gaussian order $\sigma = 2.2$, and is offset relative to the center of the circular spot by 30% of the initial target radius toward the target’s equator. The addition of this secondary ellipse directs more energy toward the equator. Finally, this spot redesign also uses a spot masking that effectively redistributes back onto target laser energy that would otherwise be lost over the target horizon as a result of the beam repointing. This is done at time $t = 0$ for all beams; however, the beam profile is modified only slightly in the polar and mid-latitude beams because of their more-moderate repointing angles. The resulting beam profiles are shown in Fig. 133.8.

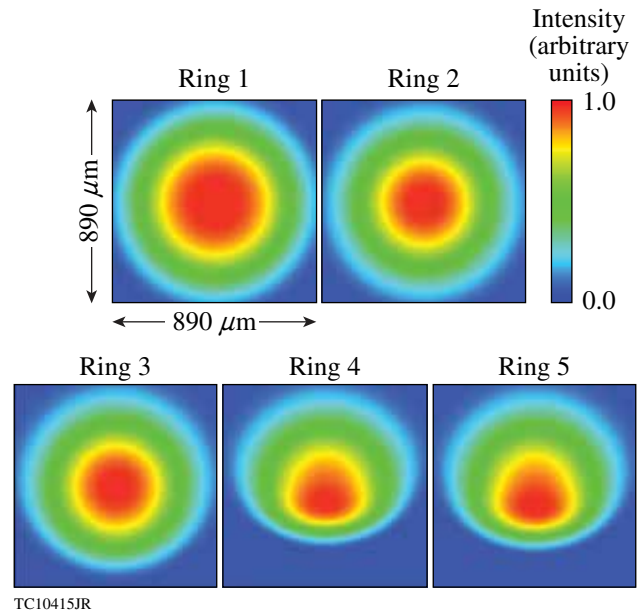


Figure 133.8

Laser-spot profiles for the split-quad polar-drive (PD) design. Laser intensity is plotted in arbitrary units with respect to position. Each box is approximately 890 μm square.

Finally, the beam powers of each ring are optimized to produce a more-uniform implosion. The beam power versus time for each ring is plotted in Fig. 133.9, along with the 1-D design pulse (black dashed line). The beams from Ring 1 are grouped together using a single laser pulse shape and are labeled the “polar.” The Ring-2 and Ring-3 beams share a second pulse shape and are labeled the “mid-latitude” beams. The Ring-4 and Ring-5 beams comprise the final grouping (“equatorial”

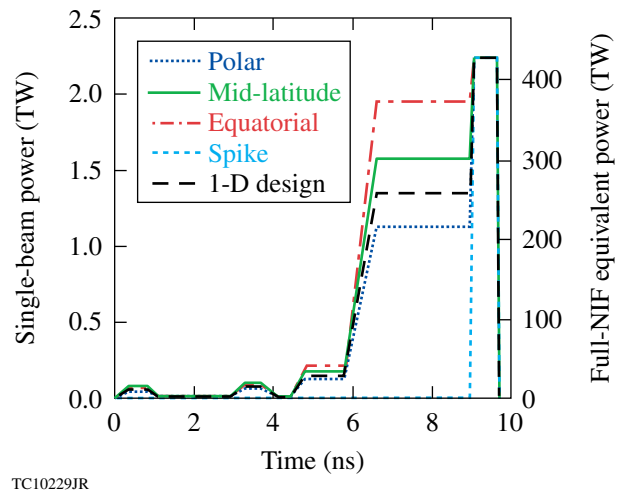


Figure 133.9

Laser pulse shapes for the split-quad PD design for each grouping of beams.

beams), all using a third pulse shape. Initial polar-drive SI simulations indicated that the final capsule symmetry is much more dependent on the compression-beam geometry than the spike-beam geometry. As such, in this design, no repointing of the shock beams in the remaining 48 half-quads was done to minimize refractive losses. The spike-beam profiles, therefore, are circular with the same super-Gaussian order $\sigma = 2.2$ as the main-drive beams. Since symmetry is largely unaffected by the spike beams, each ignitor beam has a pulse shape exactly as in 1-D for all rings, as is shown in Fig. 133.9.

This 2-D PD design uses a total of 760 kJ of laser energy. Additional input laser energy compared to the 689 kJ of the 1-D design is required to offset the enhanced refractive losses of the repointed beams caused by their higher impact parameters as well as the loss in ablative drive efficiency in those same beams as a result of the ray turning points and the position of peak absorption lying farther away from the ablation front. The maximum laser energy in any single beam is 7.4 kJ. For reference, the NIF is rated at 1.8 MJ (9.4 kJ per beam) and has already demonstrated this energy level. The simulated target density and temperature profiles at peak compression, shortly before the onset of ignition, are shown in Fig. 133.10. This target achieves a 2-D simulated gain of 52.

Recently, comparisons between OMEGA experimental data and 1-D simulations have indicated the need for implementing a numerical model of nonlocal heat transport combined with a

model of cross-beam energy transfer (CBET)⁸³ due to stimulated Brillouin scattering. While nonlocal effects and CBET are anticipated to affect laser coupling and symmetry in this target to some extent, both the nonlocal transport⁸⁴ and CBET⁸⁵ models developed recently for *DRACO* in 2-D were being tested at the time of this publication. Therefore, these simulations all use flux-limited Spitzer heat transport with a flux-limiter value of 0.06 with no cross-beam model. Given that this target design is well below the energy and power limits of the NIF, it may be possible to recover lost energy coupling caused by CBET by increasing laser power and energy. Symmetry can likewise be recovered by tuning in future simulations with the added physics packages and through experiment.

Several robustness studies were performed on this PD design to evaluate the additional contributions to compression nonuniformity caused by both capsule asymmetries and laser system uncertainties. Unless otherwise specified, these simulations were performed in a half-sphere geometry and include all even perturbation modes from $\ell = 2$ to $\ell = 50$ with a minimum grid resolution of 12 cells per smallest-wavelength mode in the transverse direction. Capsule asymmetry studies include outer-surface roughness of the plastic ablator, inner-shell-surface roughness from DT ice layering, as well as target offset due to mispositioning of the target relative to the center of beam convergence. Modeled laser system uncertainties include random beam-mispointing errors, beam-to-beam mistiming of the laser pulse, power imbalance between beams, and laser speckle and imprint from the phase plates, including beam smoothing using multi-FM SSD. Each of the capsule nonuniformity sources has been characterized experimentally in NIF-scale or OMEGA-scale capsules, and laser system uncertainty⁶⁸ on the NIF is well quantified.

Robustness to capsule nonuniformities was found to exceed NIF specifications and achieved values. Each of the following sources of nonuniformity was added to the PD capsule design individually and varied in magnitude to assess the capsule's sensitivity to the perturbation source: capsule outer-surface roughness, inner-surface DT-ice roughness, target offset from target chamber center (TCC), beam-to-beam mispointing and mistiming, and laser power balance between beams. Note that root-mean-square (rms) values in laser parameters are not systematic variations from the design specifications, but rather indicate statistical deviations of individual beams from the intended design.

Outer-surface roughness on NIF-scale capsules has been quantified as 115-nm rms with a spectrum approximated by the

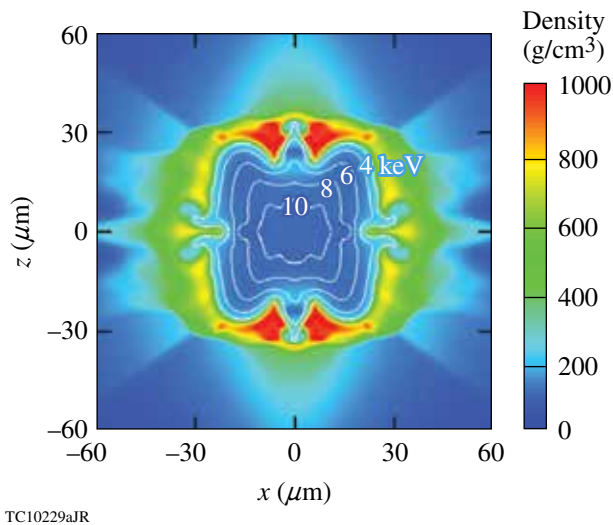


Figure 133.10
Simulated density contour plot of the 2-D split-quad PD design at the onset of ignition. Temperature contours are plotted with white lines. The target gain is 52.

formula given in Eq. (2) of Ref. 86. Simulations of this polar-drive SI design with this outer-surface roughness spectrum indicate that the target can withstand outer-surface roughness up to $5\times$ this NIF specification, or up to 575-nm rms, and still achieve ignition. The NIF specification for the inner DT-ice surface roughness is $1\text{-}\mu\text{m}$ rms, and cryogenic DT-layered OMEGA capsules have routinely demonstrated this level of uniformity.⁸⁷ These simulations indicate that the SI design tolerates over $5\text{-}\mu\text{m}$ -rms inner-surface ice roughness. Target offset was modeled in a full-sphere geometry, resolving modes $\ell = 1$ to $\ell = 50$. This capsule ignited with a target offset of up to $25\ \mu\text{m}$ — $2.5\times$ greater than the NIF specification of $10\ \mu\text{m}$. Figure 133.11 shows the predicted density and temperature profiles for this $25\text{-}\mu\text{m}$ -offset implosion. One can see that the hot spot has been pushed away from the capsule's original position, and that the hot-spot displacement is in the same direction as the initial target offset from TCC. This is expected as a result of the increased laser intensity on the side of the capsule closer to TCC. With a $25\text{-}\mu\text{m}$ offset, the gain of this target is 56.

Robustness to laser system uncertainties likewise exceed NIF specifications with ignition indicated for beam-mispointing errors up to $100\text{-}\mu\text{m}$ rms and beam-to-beam mistiming up to 100-ps rms [for comparison, the NIF specifications are $50\text{-}\mu\text{m}$ mispointing and 30-ps mistiming (see Ref. 67)]. The NIF has demonstrated 8% rms quad-to-quad power imbalance,

corresponding to a 2% rms illumination nonuniformity on target (see Ref. 67). In a split-quad beam configuration, care should be taken when pairing beams within a quad, given that the power output of beams within a quad varies significantly. This variation is systematic, however, due to a design variation in the thickness of the frequency-conversion crystals and can be minimized in a split-quad configuration by consistently choosing the same beams in each of the drive quads. Therefore, effectively for this target design, the NIF-specified power imbalance between half-quads is $\sim 11\%$ rms, a factor of $\sqrt{2}$ higher due to the fact that half of the NIF beams are used. Simulations indicate that the SI target will ignite with power imbalance up to 15% rms between half-quads.

A full nonuniformity simulation including all of these sources of nonuniformity at the NIF specifications was performed. This simulation included expected levels of laser imprint on the NIF caused by phase-plate speckle with the multi-FM-SSD smoothing parameters used in Ref. 77. This simulation, which was performed on a full sphere and resolved modes from $\ell = 1$ to $\ell = 100$, indicated a target gain of 38.

As mentioned earlier, SI with a full-quad PD beam configuration is more likely to be fielded on the NIF in the near term. Therefore, a full-quad PD beam configuration for the same capsule design has been developed. As in Ref. 88, all four quads from the 30° beams (Ring 1) and half of the quads from the 44.5° and 50° beams (Rings 2 and 3, respectively) are used for the main compression drive, while the other quads are used for the ignitor shock pulse. The main-drive beams are repointed as outlined in Table 133.IV. Each of these three rings of beams has a separate laser pulse-shape history. The pulse shapes for each ring are detailed in Fig. 133.12, with the 1-D design pulse shown for reference by the dashed line. Ring 1 comprises the polar beams, Ring 2 the mid-latitude beams, and Ring 3 the equatorial beams. As with the split-quad design, no repointing was considered for the shock beams, and the pulse shape is the same as the 1-D design. Simulations of this target design indicate a gain of 51. A density and temperature plot at the onset of ignition (Fig. 133.13) shows that the target exhibits

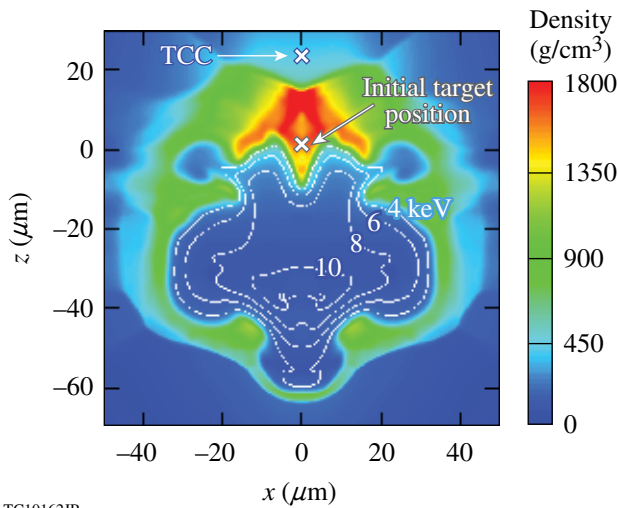


Figure 133.11 Simulated density contour plot of the 2-D split-quad PD design with an initial $25\text{-}\mu\text{m}$ target offset. The plot is shown at the onset of ignition. Temperature contours are plotted with white lines. For reference, the position of the target chamber center (TCC) and the initial target position are indicated. The target gain is 56.

Table 133.IV: Full-quad PD beam-repointing angles for the main-drive beams given by beam port location.

Beam port angle ($^\circ$)	Repointing angle on target ($^\circ$)
30.0	25.0
44.5	59.0
50.0	85.0

similar shell integrity compared to the split-quad design shown in Fig. 133.10.

Further optimization and robustness studies on this full-quad design are underway. Beam configurations that offer different repointings of beams within a single quad, as in Ref. 88, are also being considered to improve drive symmetry. Simulations with the nonlocal heat transport and CBET models must be performed, and an accounting for laser backscatter caused by LPI should be included. In addition, hot-electron

preheat effects must be modeled in the 2-D simulations. It is also anticipated that 3-D effects will be somewhat larger in the full-quad design than in the split-quad design because of the smaller number of azimuthal beam ports used during compression, and, as such, 3-D PD simulations must be performed in the future.

Conclusion

A polar-drive SI design for the National Ignition Facility has been developed within the NIF Laser System specifications. The target implosion velocity is higher than for standard SI designs to account for laser power limitations on the NIF. The proposed target ignites in 1-D simulations with an ITF_{1-D} of 4.1 using 700 kJ of input laser energy. Excellent robustness in 1-D to shock mistiming and initial gas density is predicted. Hot-electron energy coupling during the spike pulse is shown to have a positive effect on target margin at hot-electron temperatures up to 150 keV and below 20% of the incident spike laser energy.

Two-dimensional PD simulations including a 3-D laser ray-trace modeling of NIF beams and using either a split-quad or a full-quad beam configuration predict good shell uniformity and ignition with gains above 50 using 750 kJ of laser energy. PD target robustness has been shown to be excellent with respect to individual nonuniformity sources. Simulations of the split-quad PD design including all anticipated levels of system uncertainty and capsule and laser nonuniformity predict a gain of 38.

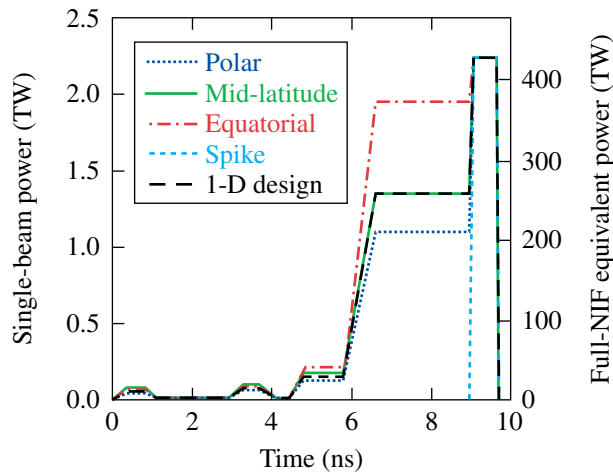
This target may be imploded on the NIF using the proposed full-quad PD beam configuration in a relatively short time frame, requiring only minor modifications to the NIF system. These modifications include the incorporation of 1-D multi-FM SSD beam smoothing, the manufacture of specially tailored laser phase plates, the introduction of polarization plates for polarization smoothing, and the development of a PD target insertion cryostat.

ACKNOWLEDGMENT

The authors thank L. J. Perkins, A. J. Schmitt, X. Ribeyre, and S. Atzeni for many enlightening discussions. This work was supported by the U.S. Department of Energy Office of Inertial Confinement Fusion under Cooperative Agreement Nos. DE-FC52-08NA28302 and DE-FC02-04ER54789, the University of Rochester, and the New York State Energy Research and Development Authority. The support of DOE does not constitute an endorsement by DOE of the views expressed in this article.

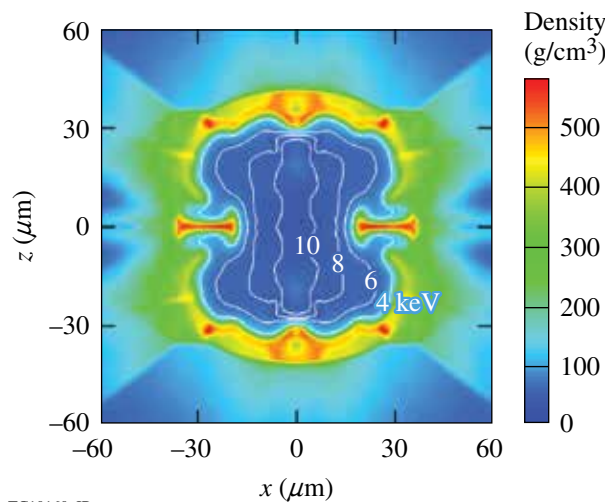
REFERENCES

1. S. Atzeni and J. Meyer-ter-Vehn, *The Physics of Inertial Fusion: Beam Plasma Interaction, Hydrodynamics, Hot Dense Matter*, International Series of Monographs on Physics (Clarendon Press, Oxford, 2004).



TC10160JR

Figure 133.12 Laser pulse shapes for the full-quad PD design for each grouping of beams.



TC10160aJR

Figure 133.13 Simulated density contour plot of the 2-D full-quad PD design at the onset of ignition. Temperature contours are plotted with white lines. The target gain is 51.

2. R. Betti, C. D. Zhou, K. S. Anderson, L. J. Perkins, W. Theobald, and A. A. Solodov, *Phys. Rev. Lett.* **98**, 155001 (2007).
3. N. G. Basov, S. Yu. Gus'kov, and L. P. Feokistov, *J. Sov. Laser Res.* **13**, 396 (1992).
4. M. Tabak *et al.*, *Phys. Plasmas* **1**, 1626 (1994).
5. V. A. Shcherbakov, *Sov. J. Plasma Phys.* **9**, 240 (1983).
6. V. A. Shcherbakov, presented at the XXXII Conference on Plasma Physics and CF, Zvenigorod, Moscow, 14–18 February 2005.
7. M. Lafon, X. Ribeyre, and G. Schurtz, *Phys. Plasmas* **17**, 052704 (2010).
8. G. Schurtz, X. Ribeyre, and M. Lafon, *J. Phys.: Conf. Ser.* **244**, 022013 (2010).
9. R. Nora and R. Betti, *Phys. Plasmas* **18**, 082710 (2011).
10. X. Ribeyre, V. T. Tikhonchuk, J. Breil, M. Lafon, and E. Le Bel, *Phys. Plasmas* **18**, 102702 (2011).
11. L. J. Perkins, R. Betti, K. N. LaFortune, and W. H. Williams, *Phys. Rev. Lett.* **103**, 045004 (2009).
12. X. Ribeyre, M. Lafon, G. Schurtz, M. Olazabal-Loume, J. Breil, S. Galera, and S. Weber, *Plasma Phys. Control. Fusion* **51**, 124030 (2009).
13. A. J. Schmitt, J. W. Bates, S. P. Obenschain, S. T. Zalesak, D. E. Fyfe, and R. Betti, *Fusion Sci. Technol.* **56**, 377 (2009).
14. A. J. Schmitt *et al.*, *Phys. Plasmas* **17**, 042701 (2010).
15. J. W. Bates *et al.*, *High Energy Density Phys.* **6**, 128 (2010).
16. B. Canaud and M. Temporal, *New J. Phys.* **12**, 043037 (2010).
17. S. Atzeni *et al.*, *Nucl. Fusion* **49**, 055008 (2009).
18. X. Ribeyre *et al.*, *Plasma Phys. Control. Fusion* **51**, 015013 (2009).
19. M. Temporal *et al.*, *Plasma Phys. Control. Fusion* **53**, 124008 (2011).
20. S. Atzeni, A. Schiavi, and A. Marocchino, *Plasma Phys. Control. Fusion* **53**, 035010 (2011).
21. M. Hohenberger, W. Theobald, S. X. Hu, K. S. Anderson, R. Betti, T. R. Boehly, A. Casner, D. E. Fratanduono, M. Lafon, D. D. Meyerhofer, R. Nora, X. Ribeyre, T. C. Sangster, G. Schurtz, W. Seka, C. Stoeckl, and B. Yaakobi, "Shock-Ignition Experiments with Planar Targets on OMEGA," submitted to *Physical Review Letters*.
22. R. Florido, R. C. Mancini, T. Nagayama, R. Tommasini, J. A. Delettrez, S. P. Regan, and B. Yaakobi, *Rev. Sci. Instrum.* **81**, 10E307 (2010).
23. W. Theobald, R. Betti, C. Stoeckl, K. S. Anderson, J. A. Delettrez, V. Yu. Glebov, V. N. Goncharov, F. J. Marshall, D. N. Maywar, R. L. McCrory, D. D. Meyerhofer, P. B. Radha, T. C. Sangster, W. Seka, D. Shvarts, V. A. Smalyuk, A. A. Solodov, B. Yaakobi, C. D. Zhou, J. A. Frenje, C. K. Li, F. H. Séguin, R. D. Petrasso, and L. J. Perkins, *Phys. Plasmas* **15**, 056306 (2008).
24. T. R. Boehly, D. L. Brown, R. S. Craxton, R. L. Keck, J. P. Knauer, J. H. Kelly, T. J. Kessler, S. A. Kumpan, S. J. Loucks, S. A. Letzring, F. J. Marshall, R. L. McCrory, S. F. B. Morse, W. Seka, J. M. Soures, and C. P. Verdon, *Opt. Commun.* **133**, 495 (1997).
25. O. Klimo *et al.*, *Phys. Plasmas* **18**, 082709 (2011).
26. O. Klimo *et al.*, *Plasma Phys. Control. Fusion* **52**, 055013 (2010).
27. W. Theobald, K. S. Anderson, R. Betti, R. S. Craxton, J. A. Delettrez, J. A. Frenje, V. Yu. Glebov, O. V. Gotchev, J. H. Kelly, C. K. Li, A. J. Mackinnon, F. J. Marshall, R. L. McCrory, D. D. Meyerhofer, J. F. Myatt, P. A. Norreys, P. M. Nilson, P. K. Patel, R. D. Petrasso, P. B. Radha, C. Ren, T. C. Sangster, W. Seka, V. A. Smalyuk, A. A. Solodov, R. B. Stephens, C. Stoeckl, and B. Yaakobi, *Plasma Phys. Control. Fusion* **51**, 124052 (2009).
28. W. Theobald, R. Nora, M. Lafon, A. Casner, X. Ribeyre, K. S. Anderson, R. Betti, J. A. Delettrez, J. A. Frenje, V. Yu. Glebov, O. V. Gotchev, M. Hohenberger, S. X. Hu, F. J. Marshall, D. D. Meyerhofer, T. C. Sangster, G. Schurtz, W. Seka, V. A. Smalyuk, C. Stoeckl, and B. Yaakobi, *Phys. Plasmas* **19**, 102706 (2012).
29. S. Depierreux, C. Goyon, K. Lewis, H. Bandulet, D. T. Michel, G. Loisel, V. Yahia, V. Tassin, C. Stenz, N. G. Borisenko, W. Nazarov, J. Limpouch, P. E. Masson Laborde, P. Loiseau, M. Casanova, Ph. Nicolaï, S. Hüller, D. Pesme, C. Riconda, V. T. Tikhonchuk, and C. Labaune, *Plasma Phys. Control. Fusion* **53**, 124034 (2011).
30. R. Betti, W. Theobald, C. D. Zhou, K. S. Anderson, P. W. McKenty, S. Skupsky, D. Shvarts, V. N. Goncharov, J. A. Delettrez, P. B. Radha, T. C. Sangster, C. Stoeckl, and D. D. Meyerhofer, *J. Phys., Conf. Ser.* **112**, 022024 (2008).
31. G. H. Miller, E. I. Moses, and C. R. Wuest, *Opt. Eng.* **43**, 2841 (2004).
32. *LLE Review Quarterly Report* **33**, 1, Laboratory for Laser Energetics, University of Rochester, Rochester, NY, LLE Document No. DOE/DP/40200-65, NTIS Order No. DE88008065 (1987). (Copies may be obtained from the National Technical Information Service, Springfield, VA 22161.)
33. Y. Kato *et al.*, *Phys. Rev. Lett.* **53**, 1057 (1984).
34. *LLE Review Quarterly Report* **114**, 73, Laboratory for Laser Energetics, University of Rochester, Rochester, NY, LLE Document No. DOE/NA/28302-826, OSTI ID 93524 (2008).
35. S. Skupsky, R. W. Short, T. Kessler, R. S. Craxton, S. Letzring, and J. M. Soures, *J. Appl. Phys.* **66**, 3456 (1989).
36. D. S. Clark, S. W. Haan, and J. D. Salmonson, *Phys. Plasmas* **15**, 056305 (2008).
37. P. Y. Chang, R. Betti, B. K. Spears, K. S. Anderson, J. Edwards, M. Fatenejad, J. D. Lindl, R. L. McCrory, R. Nora, and D. Shvarts, *Phys. Rev. Lett.* **104**, 135002 (2010).
38. B. K. Spears *et al.*, *Phys. Plasmas* **19**, 056316 (2012).
39. P. B. Radha, V. N. Goncharov, T. J. B. Collins, J. A. Delettrez, Y. Elbaz, V. Yu. Glebov, R. L. Keck, D. E. Keller, J. P. Knauer, J. A. Marozas, F. J.

- Marshall, P. W. McKenty, D. D. Meyerhofer, S. P. Regan, T. C. Sangster, D. Shvarts, S. Skupsky, Y. Srebro, R. P. J. Town, and C. Stoeckl, *Phys. Plasmas* **12**, 032702 (2005).
40. R. Betti, K. Anderson, V. N. Goncharov, R. L. McCrory, D. D. Meyerhofer, S. Skupsky, and R. P. J. Town, *Phys. Plasmas* **9**, 2277 (2002).
 41. C. D. Zhou and R. Betti, *Phys. Plasmas* **14**, 072703 (2007).
 42. J. Kline, *Bull. Am. Phys. Soc.* **57**, 200 (2012).
 43. J. Delettrez and E. B. Goldman, Laboratory for Laser Energetics, University of Rochester, Rochester, NY, LLE Report No. 36 (1976).
 44. B. I. Bennett *et al.*, Los Alamos National Laboratory, Los Alamos, NM, Report LA-7130 (1978).
 45. R. C. Malone, R. L. McCrory, and R. L. Morse, *Phys. Rev. Lett.* **34**, 721 (1975).
 46. V. N. Goncharov, J. P. Knauer, P. W. McKenty, P. B. Radha, T. C. Sangster, S. Skupsky, R. Betti, R. L. McCrory, and D. D. Meyerhofer, *Phys. Plasmas* **10**, 1906 (2003).
 47. K. Anderson and R. Betti, *Phys. Plasmas* **10**, 4448 (2003).
 48. K. Anderson and R. Betti, *Phys. Plasmas* **11**, 5 (2004).
 49. R. Betti, K. Anderson, J. Knauer, T. J. B. Collins, R. L. McCrory, P. W. McKenty, and S. Skupsky, *Phys. Plasmas* **12**, 042703 (2005).
 50. Lord Rayleigh, in *Scientific Papers* (Cambridge University Press, Cambridge, England, 1900), Vol. II, pp. 200–207.
 51. G. Taylor, *Proc. R. Soc. London Ser. A* **201**, 192 (1950).
 52. S. E. Bodner, *Phys. Rev. Lett.* **33**, 761 (1974).
 53. H. Takabe *et al.*, *Phys. Fluids* **28**, 3676 (1985).
 54. R. Betti, V. N. Goncharov, R. L. McCrory, and C. P. Verdon, *Phys. Plasmas* **5**, 1446 (1998).
 55. J. P. Knauer, K. Anderson, R. Betti, T. J. B. Collins, V. N. Goncharov, P. W. McKenty, D. D. Meyerhofer, P. B. Radha, S. P. Regan, T. C. Sangster, V. A. Smalyuk, J. A. Frenje, C. K. Li, R. D. Petrasso, and F. H. Séguin, *Phys. Plasmas* **12**, 056306 (2005).
 56. V. N. Goncharov, T. C. Sangster, T. R. Boehly, S. X. Hu, I. V. Igumenshchev, F. J. Marshall, R. L. McCrory, D. D. Meyerhofer, P. B. Radha, W. Seka, S. Skupsky, C. Stoeckl, D. T. Casey, J. A. Frenje, and R. D. Petrasso, *Phys. Rev. Lett.* **104**, 165001 (2010).
 57. J. A. Marozas, J. D. Zuegel, and T. J. B. Collins, *Bull. Am. Phys. Soc.* **55**, 294 (2010).
 58. N. Metzler, A. L. Velikovich, and J. H. Gardner, *Phys. Plasmas* **6**, 3283 (1999).
 59. N. Metzler *et al.*, *Phys. Plasmas* **9**, 5050 (2002).
 60. N. Metzler *et al.*, *Phys. Plasmas* **10**, 1897 (2003).
 61. T. J. B. Collins and S. Skupsky, *Phys. Plasmas* **9**, 275 (2002).
 62. T. J. B. Collins, J. P. Knauer, R. Betti, T. R. Boehly, J. A. Delettrez, V. N. Goncharov, D. D. Meyerhofer, P. W. McKenty, S. Skupsky, and R. P. J. Town, *Phys. Plasmas* **11**, 1569 (2004).
 63. A. B. Iskakov *et al.*, *Phys. Rev. E* **61**, 842 (2000).
 64. E. Krouský *et al.*, *Laser Part. Beams* **18**, 87 (2000).
 65. V. A. Smalyuk, V. N. Goncharov, K. S. Anderson, R. Betti, R. S. Craxton, J. A. Delettrez, D. D. Meyerhofer, S. P. Regan, and T. C. Sangster, *Phys. Plasmas* **14**, 032702 (2007).
 66. J. A. Marozas, LLE, private communication (2012).
 67. C. J. Stolz, *Phil. Trans. R. Soc. Lond. A* **370**, 4115 (2012).
 68. A. Simon, R. W. Short, E. A. Williams, and T. Dewandre, *Phys. Fluids* **26**, 3107 (1983).
 69. W. Seka, D. H. Edgell, J. P. Knauer, J. F. Myatt, A. V. Maximov, R. W. Short, T. C. Sangster, C. Stoeckl, R. E. Bahr, R. S. Craxton, J. A. Delettrez, V. N. Goncharov, I. V. Igumenshchev, and D. Shvarts, *Phys. Plasmas* **15**, 056312 (2008).
 70. W. Seka, D. H. Edgell, J. F. Myatt, A. V. Maximov, R. W. Short, V. N. Goncharov, and H. A. Baldis, *Phys. Plasmas* **16**, 052701 (2009).
 71. D. T. Michel, A. V. Maximov, R. W. Short, S. X. Hu, J. F. Myatt, W. Seka, A. A. Solodov, B. Yaakobi, and D. H. Froula, *Phys. Rev. Lett.* **109**, 155007 (2012).
 72. J. F. Myatt, J. Zhang, V. N. Goncharov, A. V. Maximov, R. W. Short, D. F. DuBois, D. A. Russell, and H. X. Vu, *Bull. Am. Phys. Soc.* **57**, 299 (2012).
 73. C. Riconda *et al.*, *Phys. Plasmas* **18**, 092701 (2011).
 74. S. Weber *et al.*, *Phys. Rev. E* **85**, 016403 (2012).
 75. S. Skupsky, J. A. Marozas, R. S. Craxton, R. Betti, T. J. B. Collins, J. A. Delettrez, V. N. Goncharov, P. W. McKenty, P. B. Radha, T. R. Boehly, J. P. Knauer, F. J. Marshall, D. R. Harding, J. D. Kilkenny, D. D. Meyerhofer, T. C. Sangster, and R. L. McCrory, *Phys. Plasmas* **11**, 2763 (2004).
 76. J. A. Marozas, F. J. Marshall, R. S. Craxton, I. V. Igumenshchev, S. Skupsky, M. J. Bonino, T. J. B. Collins, R. Epstein, V. Yu. Glebov, D. Jacobs-Perkins, J. P. Knauer, R. L. McCrory, P. W. McKenty, D. D. Meyerhofer, S. G. Noyes, P. B. Radha, T. C. Sangster, W. Seka, and V. A. Smalyuk, *Phys. Plasmas* **13**, 056311 (2006).
 77. T. J. B. Collins, J. A. Marozas, K. S. Anderson, R. Betti, R. S. Craxton, J. A. Delettrez, V. N. Goncharov, D. R. Harding, F. J. Marshall, R. L. McCrory, D. D. Meyerhofer, P. W. McKenty, P. B. Radha, A. Shvydky, S. Skupsky, and J. D. Zuegel, *Phys. Plasmas* **19**, 056308 (2012).
 78. A. M. Cok, R. S. Craxton, and P. W. McKenty, *Phys. Plasmas* **15**, 082705 (2008).

79. F. J. Marshall, R. S. Craxton, M. J. Bonino, R. Epstein, V. Yu. Glebov, D. Jacobs-Perkins, J. P. Knauer, J. A. Marozas, P. W. McKenty, S. G. Noyes, P. B. Radha, W. Seka, S. Skupsky, and V. A. Smalyuk, *J. Phys. IV France* **133**, 153 (2006).
80. R. S. Craxton, F. J. Marshall, M. J. Bonino, R. Epstein, P. W. McKenty, S. Skupsky, J. A. Delettrez, I. V. Igumenshchev, D. W. Jacobs-Perkins, J. P. Knauer, J. A. Marozas, P. B. Radha, and W. Seka, *Phys. Plasmas* **12**, 056304 (2005).
81. R. S. Craxton and D. W. Jacobs-Perkins, *Phys. Rev. Lett.* **94**, 095002 (2005).
82. L. J. Perkins, LLNL, private communication (2011).
83. I. V. Igumenshchev, W. Seka, D. H. Edgell, D. T. Michel, D. H. Froula, V. N. Goncharov, R. S. Craxton, L. Divol, R. Epstein, R. Follett, J. H. Kelly, T. Z. Kosc, A. V. Maximov, R. L. McCrory, D. D. Meyerhofer, P. Michel, J. F. Myatt, T. C. Sangster, A. Shvydky, S. Skupsky, and C. Stoeckl, *Phys. Plasmas* **19**, 056314 (2012).
84. G. A. Moses, LANL, private communication (2012).
85. J. A. Marozas and T. J. B. Collins, *Bull. Am. Phys. Soc.* **57**, 344 (2012).
86. P. W. McKenty, V. N. Goncharov, R. P. J. Town, S. Skupsky, R. Betti, and R. L. McCrory, *Phys. Plasmas* **8**, 2315 (2001).
87. T. C. Sangster, R. Betti, R. S. Craxton, J. A. Delettrez, D. H. Edgell, L. M. Elasky, V. Yu. Glebov, V. N. Goncharov, D. R. Harding, D. Jacobs-Perkins, R. Janezic, R. L. Keck, J. P. Knauer, S. J. Loucks, L. D. Lund, F. J. Marshall, R. L. McCrory, P. W. McKenty, D. D. Meyerhofer, P. B. Radha, S. P. Regan, W. Seka, W. T. Shmayda, S. Skupsky, V. A. Smalyuk, J. M. Soures, C. Stoeckl, B. Yaakobi, J. A. Frenje, C. K. Li, R. D. Petrasso, F. H. Séguin, J. D. Moody, J. A. Atherton, B. D. MacGowan, J. D. Kilkenny, T. P. Bernat, and D. S. Montgomery, *Phys. Plasmas* **14**, 058101 (2007).
88. L. Tucker, *2010 Summer Research Program for High School Juniors at the University of Rochester's Laboratory for Laser Energetics*, University of Rochester, Rochester, NY, LLE Report No. 365, LLE Document No. DOE/NA/28302-1000 (2011).